Chapter-5

Study of Isomorphic Phase Transition in non-Perovskites Green $CsSnI_3$ and its impact on Hysteresis

1. *Observation of isomorphic phase transition in non-perovskite Green $CsSnI_3$,* ***Prem C. Bharti,*** *Priyanka A. Jha, Pardeep K. Jha, and Prabhakar Singh, Materialia 27, 2023, 101646*

2. *Hystersis and Pyroelectric behaviour at isomorphic transition in Green $CsSnI_3$,* ***Prem C. Bharti****, Priyanka A. Jha, Pardeep K. Jha, and Prabhakar Singh. (Communicated)*

CHAPTER 5: Study of Isomorphic Phase Transition in non-Perovskites Green $CsSnI_3$ and its impact on Hysteresis

5.1 Introduction

It has been discussed in chapter 3, $CuPbI_3$ compounds shows the variation with the change in the polarization behavior. This chapter aim to study the Isomorphic phase in $CsSnI_3$. The green polymorph of $CsSnI_3$ synthesized by cold-sintering method. The structural refinement shows the cubic T_h(m-3)-Pa$\bar{3}$ phase with paramorphic hemihedry (diacisdodecahedery) for $CsSnI_3$. The determined lattice constant is a = 12.2771(1) Å, with a corresponding cell volume of 1850.49(4) $Å^3$.The Iodine atoms do not occupy the equivalent positions and the number of molecules per unit cell is 8. Contrary to other colour polymorphs, this green $CsSnI_3$ has shown successive isomorphic phase transitions in accordance with the group–subgroup theory.

5.2 Experimental Details

The powder sample of $CsSnI_3$ was synthesized through a solid state reaction route method at room temperature in the ambient environment. For these two precursors CsI (99.9% Alfa Aesar) and SnI_2 (99% Alfa Aesar) were weighted in the stoichiometric ratio and ground for the two hours in the mortar-pestle. After grounding we found a greenish black colour powder of $CsSnI_3$. $CsSnI_3$ sample was synthesized by using the following equation —

$$CsI + SnI_2 \rightarrow CsSnI_3 \qquad (5.1)$$

Finally, powder was sintered at 280 K (ice bath condition) for 2 h. The powder was pelletized using a hydraulic press of 5 tons. The X-ray diffractogram was obtained using Rigaku Miniflex with 2θ range from 10° to 80° with step size 0.01°. The UV–Vis absorption spectrum was

obtained using JASCO V-770 spectrophotometer. The Raman spectrograph was studied in the wavenumber range of 30–1000 cm^{-1}. Differential scanning calorimetry (DSC) of the compound was conducted using SHIMADZU DSC-60 plus, 230 V. The dielectric studies were carried out using Solartron 1260 A impedance analyzer with an oscillation amplitude of 1V. Further, the impedance measurement of the studied perovskite material was done using Solartron 1260 A impedance analyzer. The details of synthesis process have already been explained in the previous chapter.

5.3 Results and Discussion

5.3.1 Structural study

Figure 5.1(a) shows the X-ray diffractograms of $CsSnI_3$ along with the reported JCPDS of $CsSnI_3$ corresponding to orthorhombic ($Pnma$) phase and it can be seen that the peaks observed at higher angle are not matching with the standard JCPDS files. The peak profile at smaller angles is also not matching with the standard JCPDS files. Then we performed the Raman study (Figure 5.1b), interestingly we got a very low intensity A_g mode at 123 cm^{-1} almost merge with background for different lasers (633 nm and 785 nm), suggesting higher symmetric phase for the crystal, contrary to its polymorphs i.e., B- and Y-$CsSnI_3$ as illustrated in inset figure by colour pattern which represents the colour polymorphs of $CsSnI_3$ on phase symmetry axis [234].

Moreover, the direct band gap of ~ 1.24 eV (Figure 5.1c) has been estimated from the UV spectra at ~295 K and it does not match with other reported polymorph of $CsSnI_3$ or its derivative compounds. Thus, we determined the crystal structure of G-$CsSnI_3$ by trial and error

method. Firstly, we tried to index with different possible crystal phases using POWDERX software.

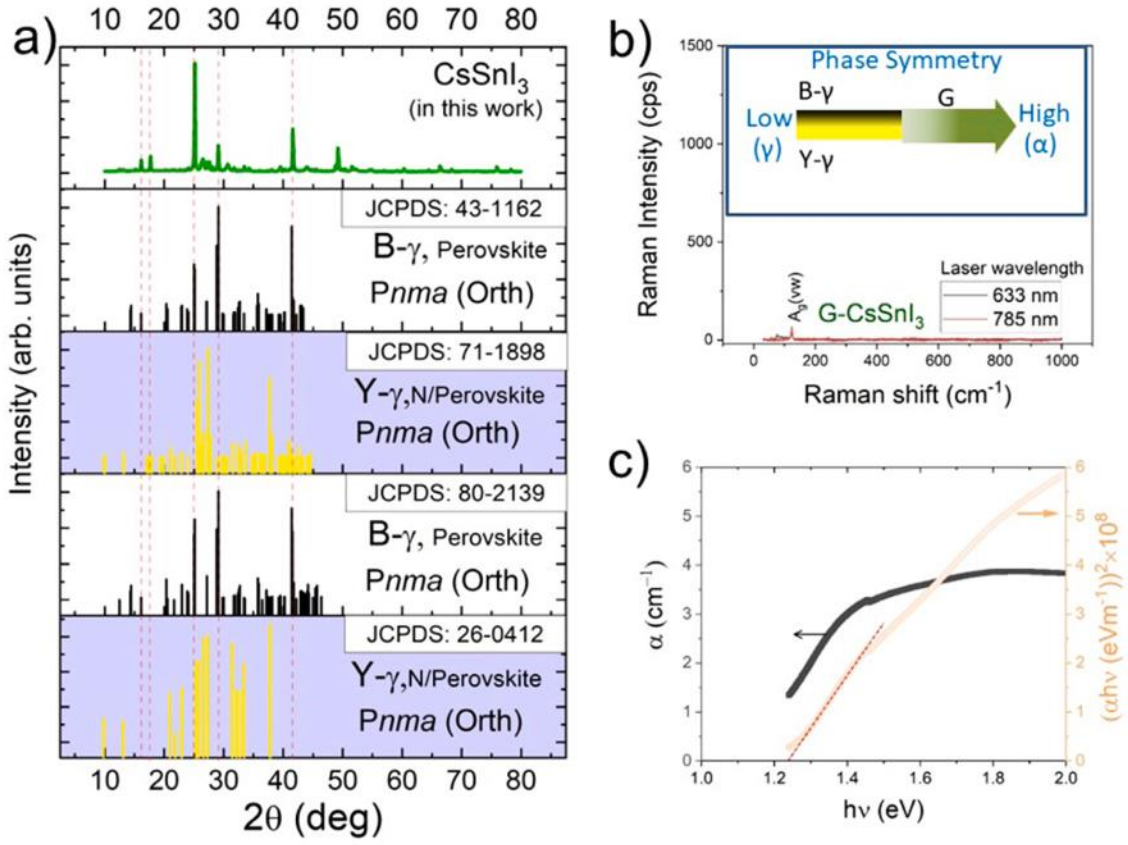

Figure 5.1 (a) XRD of green $CsSnI_3$ along with the reported JCPDS of orthorhombic-$CsSnI_3$ for Black (B-γ) and Yellow(Y-γ) polymorph, (b) Raman spectra with 633 nm and 785 nm laser, (inset) colour patterns representing the colour polymorphs of $CsSnI_3$ on phase symmetry axis, suggesting the G-$CsSnI_3$ possess high symmetry than B-γ and Y-γ polymorphs (c) Variation of absorbance and Tauc plot showing the band gap of 1.24 eV cold-sintered green $CsSnI_3$

The best match indexing is found for cubic (primitive) with the interferences as follows: reflections with 'h' even, reflections with higher intensities showed that 'h' and 'k' both are even, reflections with lower intensities showed that 'h' is even and 'k' is odd. This indexing is further confirmed by Le-Bail refinements using least square refinement in Full Prof Suite package. The Le-Bail fitting of the XRD pattern obtained at room temperature was performed

with cubic $Pa\bar{3}$ symmetry. The fitting applied the Thompson–Cox– Hastings pseudo-Voigt peak profile function, with axial divergence symmetry and instrumental correction. However, the Le-Bail refinement is also done using low symmetry viz., orthorhombic (Pnma) symmetry but better values of goodness of fit factor (χ^2) is obtained for cubic phase. Thus, from the Le-Bail refinements, it is concluded that $CsSnI_3$ is crystallized in the cubic, space group T_h (m-3). The determined lattice parameters are: a = 12.2806(1) Å with cell volume = 1852.07(2) $Å^3$. Further, Rietveld refinement has been performed to achieve with the Wyckoff positions of various known compounds such as SnI_4 , $TiBr_4$, TiI_4 , $Ni(CO)_4$ etc. (Table 5.1). But the refinement could not be achieved and gave very bad correspondence with the XRD pattern. In addition, the refinement could not be achieved with the orthorhombic phase of $CsSnI_3$. Further, through Bilbao crystallographic server, the atomic positions were taken in a combination of 4a, 4b, 8c and 24d. In this case, refinement is achieved (Figure 5.2(a)) giving better correspondence to the XRD pattern with Bragg and Rf factors of ~ 2.4 and 2.5, respectively and the goodness of factor $\chi^2 \backsim$ 2.3. The refined lattice parameters are: a = 12.2771(1) Å with cell volume = 1850.49(4) $Å^3$.

In the Patterson diagrams (Figure 5.2(b)), a pronounced maxima corresponding to Cs atom is obtained in which the ellipsoid is deformed vertically caused by several nearly equal inter and intra molecular I–I distances. The atoms do not occupy the equivalent positions. The structure comprises 8 $CsSnI_3$ units i.e., Z= 8. In Fig. 5.2(b), the basic structure is distorted tetrahedral packing of I atoms. It is observed (using Diamond software) (Figure 5.2(c)) that each Sn-atom be surrounded by equidistant I-atoms with $l_{Sn\text{-}I}$ = 2.4114 Å and $\angle\theta_{I\text{-}Sn\text{-}I}$ ~ 105.9° (Figure 5.2(d)). As the basic formula type is ABX_3 (pseudo perovskite) instead of tetrahedron formula type XBX_3 , thus forth tetrahedral arm is with $l_{Sn\text{-}Cs}$ = 6.2137(2) Å and $\angle\theta_{Cs-Sn-I}$ ~ 112.9°.It

can also be seen that the shape of the beam is deviated as can be seen through bond lengths and bond angles. The other structural parameters such as Wyckoff positions, atomic positions are provided in Table 5.1 and anisotropic thermal parameters ($Å^2$) are tabulated in Table 5.2.

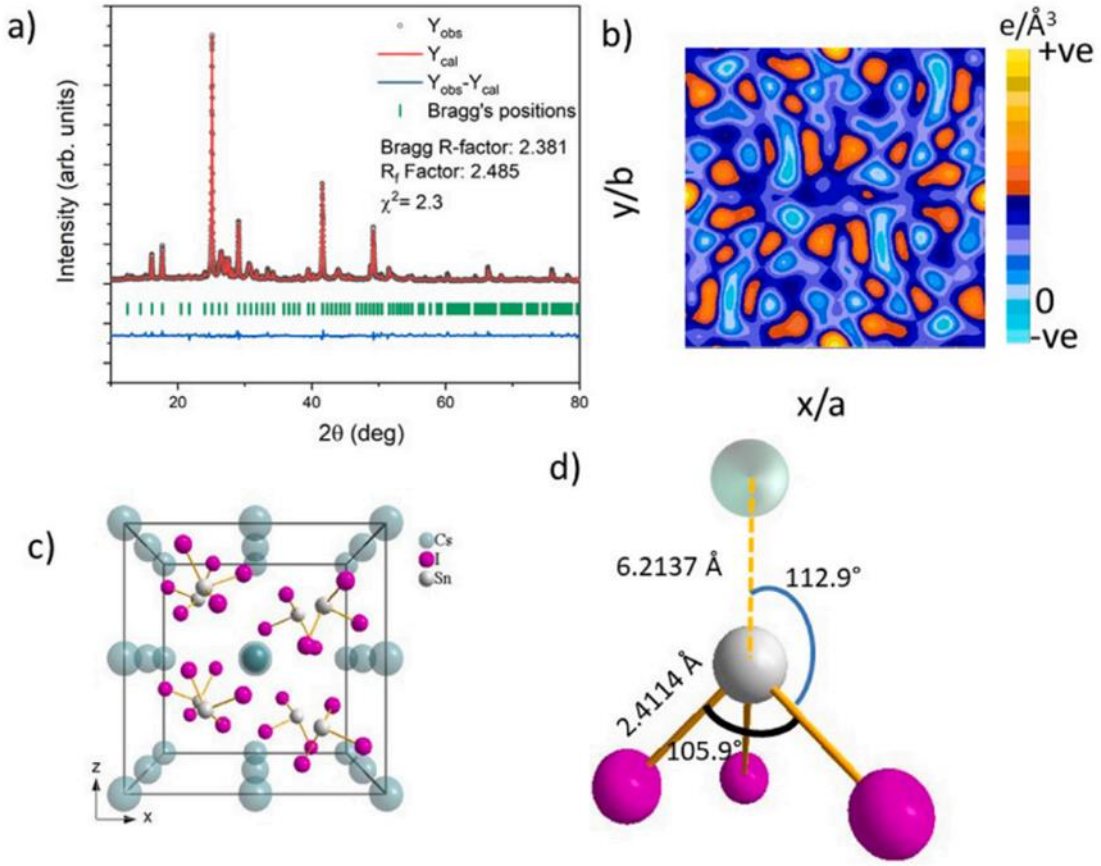

Figure 5.2 (a) Rietveld refinement of G-$CsSnI_3$ with cubic $Pa\overline{3}$ symmetry (b) electron density (Patterson) maps (c) Crystal Structure showing Z = 8 (d) Bond angle with bond length.

These parameters suggest that iodine atoms are arranged in such a way that they are crystallographically non-equivalent to each other. This is further arising from the arrangement of molecules instead of the difference in forces between Sn and I atoms. The distance is

observed to be less than 2.8 Å i.e. the sum of Bragg radii. In the ideal $Pa\bar{3}$ structure, the tetrahedral coordination is maintained.

Table 5.1 Wyckoff positions, atomic positions for G-$CsSnI_3$

Atom	**Wyckoff**	**x/a**	**y/b**	**z/c**
Cs	4a	0.0	0.0	0.0
Cs	4b	0.5	0.5	0.5
Sn	8c	0.70779	0.70779	0.70779
I	24d	-0.64420	0.44338	0.19969

Table 5.2 Anisotropic Thermal Parameters ($Å^2$)

Atom	**Wyckoff**	**U_{11}**	**U_{22}**	**U_{33}**	**U_{12}**	**U_{13}**	**U_{23}**
Cs	4a	-0.3125	-0.3125	-0.3125	0.0087	0.0087	0.0087
Cs	4b	-0.3092	-0.3092	-0.3092	0.04933	0.04933	0.04933
Sn	8c	0.04887	0.04887	0.04887	-0.1136	-0.1136	-0.1136
I	24d	0.45884	-0.3234	-0.3006	-0.0370	-0.1427	0.09667

But in the present case, (a) the tetrahedra is distorted (ii) the Iodine atoms are in non-equivalent positions and (iii) the tetrahedra translation is along a threefold axis. Thus, $CsSnI_3$ has a distorted tetrahedral packing in which I atoms are crystallographically non-equivalent. Contrary to B- and Y-$CsSnI_3$, all the above studies suggest cubic phase for G-$CsSnI_3$ at ~295 K.

From literature survey, we have summarized that B-$CsSnI_3$ polymorph shows reconstructive phase transition from cubic ($Pm\bar{3}m$)→ tetragonal (P4/mbm)→ orthorhombic (Pnam)→

(possible) monoclinic on cooling from 450 K to 250 K as illustration in two horizontal panels at top in figure 5.3(a). With the exposure to air the B-γ transforms into Y-γ. Further, Y-$CsSnI_3$ polymorph shows transformation to B-α at 425 K in an inert atmosphere [235]. To know how the transitions are occurring in G-$CsSnI_3$, we performed the temperature dependent-differential scanning calorimetry (DSC) and dielectric study in the range of (250–460 K). From, temperature dependent the second derivative of heat (Q) and permittivity (ε') plot (Figure 5.3a(i) and (ii), respectively), ambiguity at ∼418 K can be seen but the heat change as well as permittivity change is not colossal.

Interestingly, it is nearly coincident with the reported $\alpha - \beta$ transition at 426 K for B-$CsSnI_3$. However, the $\beta - \gamma$ phase transition for B- and Y-$CsSnI_3$ are completely absent in Fig. 5.3(a) while a small hump is observed at ∼372 K in the dielectric plot. The major finding is observation of a new isomorphic phase transition at ∼326 K. Two more weak peaks are occurring at 292 K and 273 K. As the XRD and Raman study suggest a cubic phase with $Pa\bar{3}$ symmetry at 295(±1) K, we need to explore the possibility of such a transition. The presence of high symmetry at 295 K suggests the transitions above this temperature must be isomorphic. It means all these transitions must be second order phase transitions which must satisfy conditions: (a) Q would be continuous and (b) must follow group– subgroup relation.

The weak and very weak peaks in $\frac{\partial^2 Q}{\partial^2 T}$ curve suggest condition (a) is satisfied here, therefore with help of group (*G)*-subgroup ($\mathcal{H}$) relation we tried to find the minimal supergroup of $Pa\bar{3}$ from the inverse $G - \mathcal{H}$ tree (Fig. 4.3(b)) [236]. Here, $P\ m3m$ is common supergroup and also with fact that the transition at 418 K is nearly similar to $\alpha - \beta$ transition at 426 K for B-$CsSnI_3$, thus we assume the supergroup at T > 418 K is ($Pm\bar{3}m$). The possible sequence of

successive isomorphic phase transitions is $Pm\bar{3}m \rightarrow Pm\bar{3} \rightarrow Ia\bar{3} \rightarrow Pa\bar{3}$ as shown in Figure 5.3(b) (by dashed line) and summarized in 5.3(a) (bottom panel).

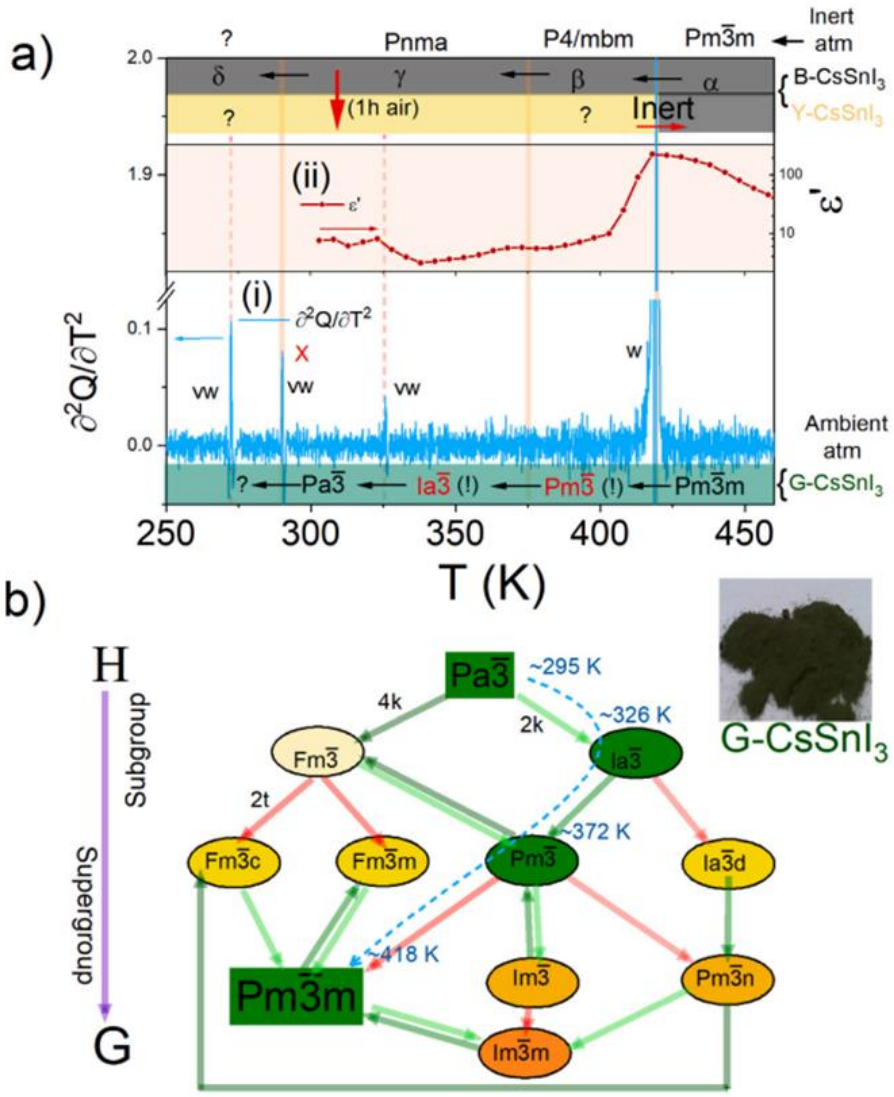

Figure 5.3 : (a) Temperature dependent (i) second derivative of heat (from DSC) and (ii) dielectric study in the range of (250–460 K) with comparative of phase transition in existing B- and Y-$CsSnI_3$ (two panels yellow and black at top) with possible transitions in G-$CsSnI_3$ (bottom panel). (Symbol & Abbreviations: ×(Red)-room temperature (here temperature at which characterization is performed), w-weak, vw-very weak) (b) inverse group (G)-subgroup ($\mathcal{H}$) relation tree for the minimal supergroup of Pa3 the possible sequence of successive isomorphic phase transitions ($Pm\bar{3}m \rightarrow Pm\bar{3} \rightarrow Ia\bar{3} \rightarrow Pa\bar{3}$) with decrease in temperature is shown by dashed line (inset: green $CsSnI_3$ powder).

5.3.2 I-V Study

Recently, we had observed an unusual isomorphic phase transition in green polymorph of $CsSnI_3$ (G-$CsSnI_3$) which is cubic ($Pa\bar{3}$) at 295 K and undergoes phase transitions at higher temperatures in the following sequence: $Pm\bar{3}m \overset{418K}{\longleftrightarrow} Pm\bar{3} \overset{372K}{\longleftrightarrow} Ia\bar{3} \overset{326K}{\longleftrightarrow} Pa\bar{3}$ [237].

We investigated the impact of these phase transitions on hysteresis and discovered pyro electricity in the G-$CsSnI_3$ sample, analogous to ferroelectric materials. Despite the sample's centrosymmetric nature suggested by macroscopic behaviour, we employed PFM, temperature-dependent dielectric measurements, impedance spectroscopy, and Raman spectroscopy. Findings indicate that local modifications in vibrational modes significantly influence the current-voltage hysteresis and conduction properties of perovskite halides, revealing the presence of local non-Centro symmetry within the globally centrosymmetric $CsSnI_3$.

In order to explore the influence on phase transition on current voltage hysteresis here we studied the temperature dependent behaviour of current voltage curve both in dark and light i.e., AM 1.5 G around the phase transition ($Ia\bar{3} \overset{372K}{\longleftrightarrow} Pa\bar{3}$) as shown in figure 5.1a. The volatile nature of PHs at higher temperature in presence of light, didn't allow us to study the higher temperature range in ambient conditions. Here, we observe that (a) in $Pa\bar{3}$ phase value of current is small but suddenly increase in $Ia\bar{3}$ phase, (b) current value always smaller in the presence of light. Then, we estimated hysteresis area (A_{Hys}) for IV curves and found that there is a sharp decrease in the A_{Hys} ($\rightarrow 0$) at phase transition. Although, in the presence of light, phase transition temperature appears to reduce by ~8 K. To understand this, we studied voltage-time and computed charge accumulated by integration of current over the cycle,

plotted normalised charge with time as shown in Figure5.5(a, b**)**. We found except 313 K, no curve is coinciding suggests internal electric field alteration. Therefore, local polarisation may have been changed and to verify this we performed Pyroelectric characterization as temperature change can alter the alignment or magnitude of these dipoles, causing a change in polarization (△P) which generate a pyroelectric current (I_{py}).

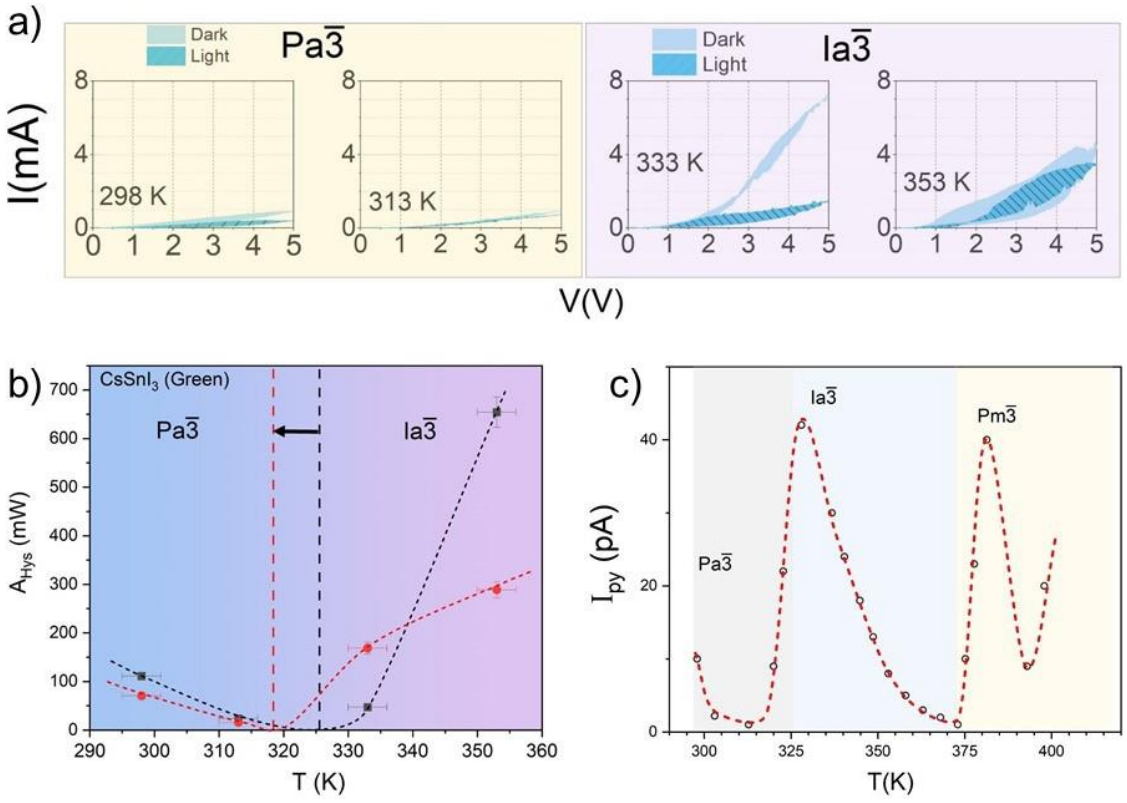

Figure 5.4 a) The I −V curves for dark and just illuminated, at 298 K, 313 K, 333 K and 353 K (b) A_{Hys} plot (c) Pyroelectric current Vs Temperature plot

The related pyroelectric coefficient (π) is given as-

$$\pi = I_{py}/\left[A\left(\frac{dT}{dt}\right)\right] \qquad (5.2)$$

where A is area of sample surface and $\frac{dT}{dt}$ is rate of heating [238][239][240][241]. Ferroelectric materials show pyroelectric response, as they have permanent dipoles, perhaps that's why ferroelectricity was assumed one of the reason behind the current voltage hysteresis problem in Perovskite Halides. The Pyroelectric current is measured (Figure 5.5c) which shows some peaks in the vicinity of phase transtion temperatures.

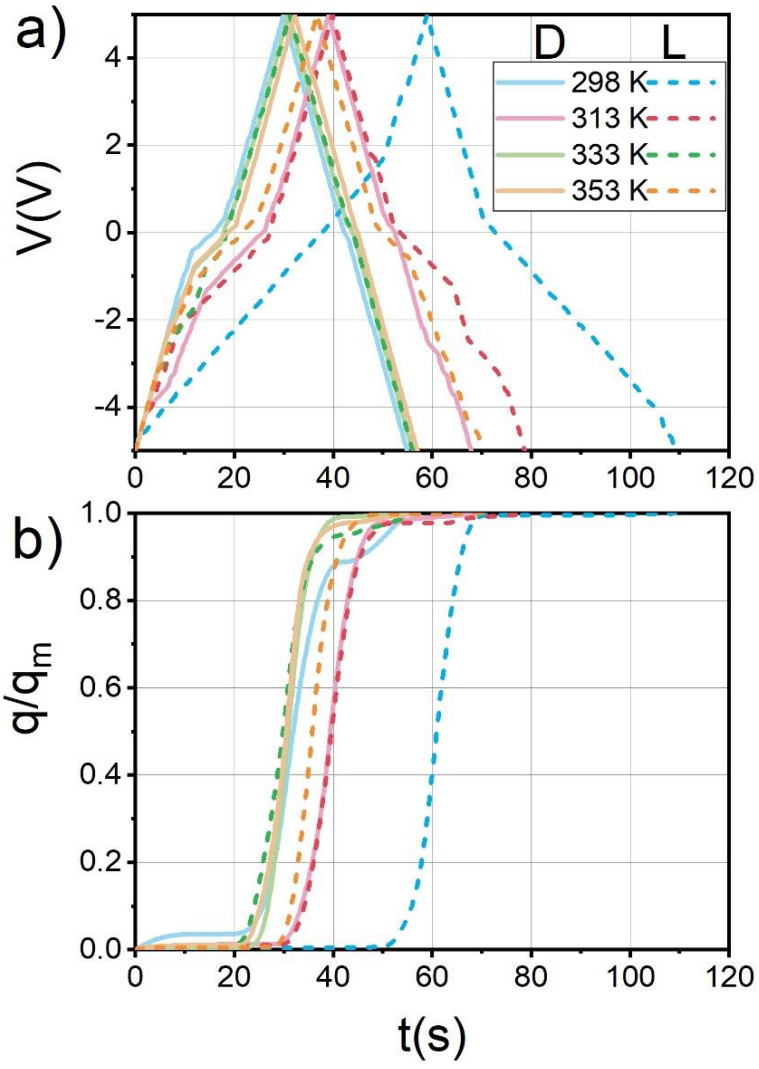

Figure 5.5 a) voltage-time curve, b) normalised charge-time over a complete cycle.

In pyroelectric materials, the internal electric dipoles are aligned in a specic direction. But here, we know that the G-$CsSnI_3$ cannot be in the ferroelectric state at ambient temperature as crystal phase is cubic at temperature, $T \geq 295$ K. Therefore, no net dipole moment due to Centro-symmetric structure. Thus if there is any change is polarization it must be due to local lattice alteration.

5.3.3 AFM study

The confirmation of the above discussion is confirmed from the electric-field dependence of the measured piezo response (Figure 5.6). For the contribution of extrinsic electrostatics, the local electromechanical measurements for possible artefacts has been observed. In Figure 5.6, the dominant effect of applied bias is to impose an oset on the measured signal in $CsSnI_3$, while keeping the contrast between entities largely unchanged. This phenomenon has also been observed in both $Cu_{0.4}In_{1.2}P_2S_6$ and $CuInP_2Se_6$ [132]. High-resolution topographic imaging of the surface did not show any signs of pinhole formation which could be an indication of dielectric breakdown. This fact, as well as reproducibility of the I-V characteristics, strongly suggests that the electro migration effect can be ruled out [133].

An atomic force microscopy tip is rastered across the surface of the sample. If leakage predominantly occurs along grain boundaries, The AFM image should reveal dark polyhedral grains surrounded by white grain boundaries, which would appear brighter as the applied voltage increases. In fact, the opposite situation occurs. This indicates that the grains have relatively low resistivity, with high-resistivity grain boundaries. Alos, the grain conduction comes in a discrete step; an individual grain suddenly “turns on” like a switch. Smaller grains generally conduct at lower voltages in accordance with Maier's theory, which suggests that

space-charge effects are more pronounced smaller grains with higher surface volume ratios as seen in Figure5.6[242].

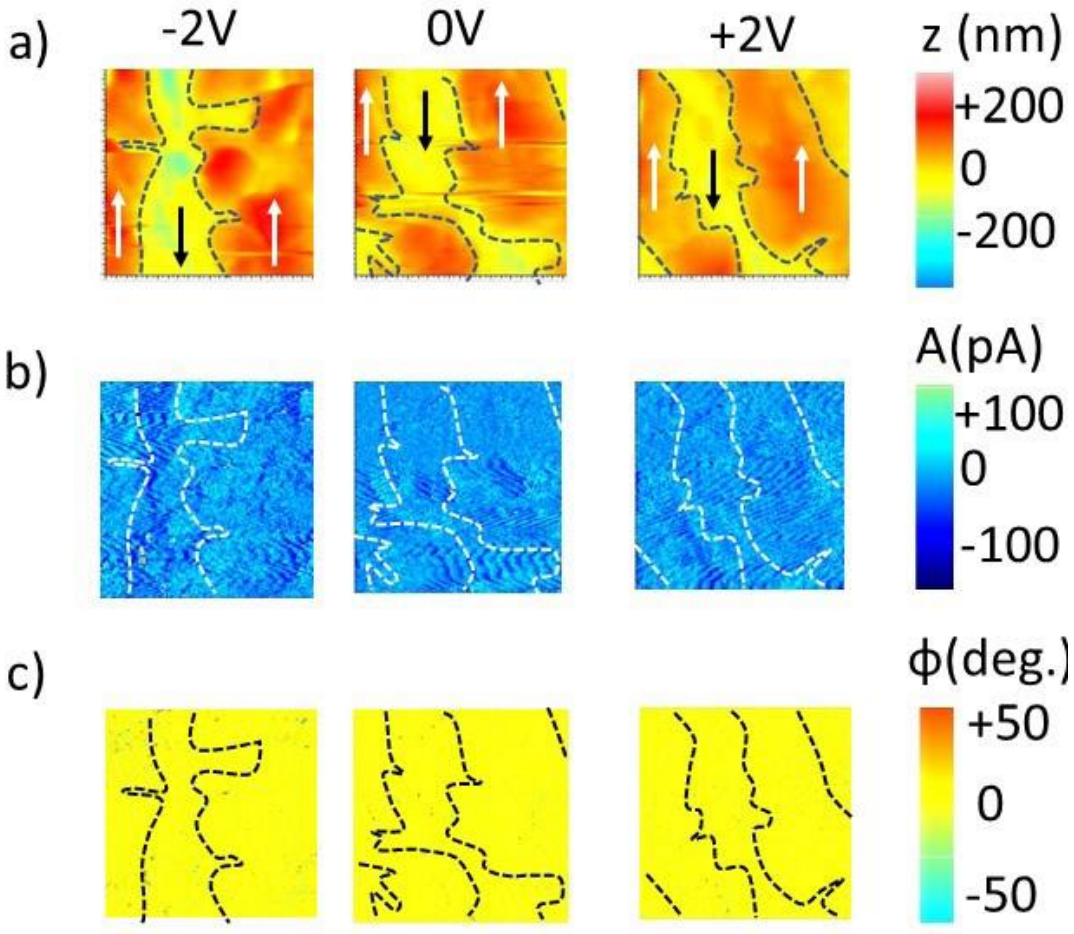

Figure 5.6. a) PFM and a resistive switching imaged by C-AFM. A change in PFM contrast correlates with the transition from low current (dark contrast) to high current (bright contrast) at 298 K but no alteration in PFM amplitude and phase is appearing suggesting absence of ferroelectric phase (b) Amplitude and (c) Phase variation with voltage**.**

In Figure 5.7, for pristine sample, exponent for grain contribution is decreasing with the increase in temperature while grain-boundary contribution has been observed after 350 K and is invariant with temperature. The value of exponent is nearly 0.1 in grain-boundary regime suggesting nearly resistive grain- boundary. However, after light fall samples showed nearly

resistive grains and exponent of grain-boundary (< 0.3) is observed to decrease with the temperature. Further, when the dipoles are freezed, then no grain-boundary contribution is observed while, bulk exponent is observed to decrease with the increase in temperature and its value if < 0.8 suggesting the accumulated charge carriers in the grain.

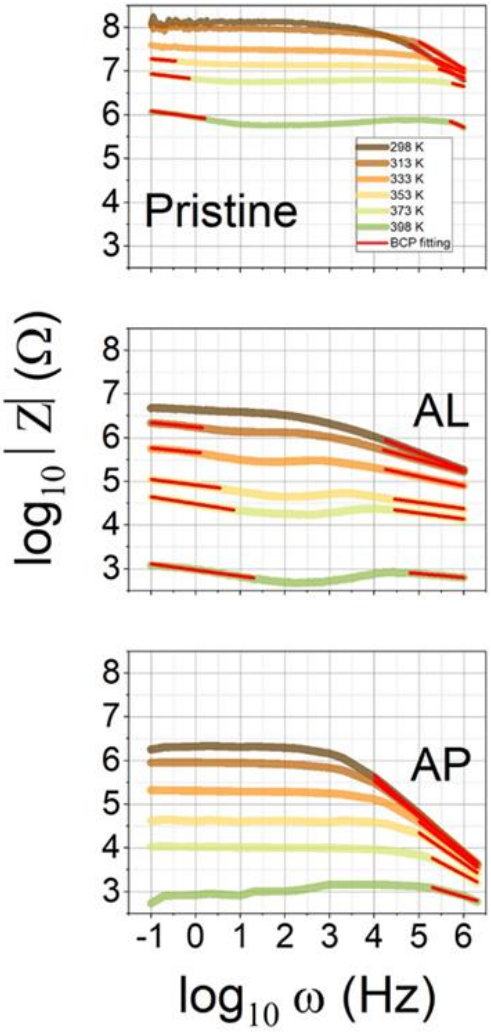

Figure 5.7 Impedance bode plots in the pristine sample, after light (AL) treatment and after poling (AP) I-V measurement.

As the charge carriers' distribution is different for bulk and grain-boundary contributions, it is important to study the relaxation time with temperature. The relaxation time is estimated

(Figure 5.8b) from permittivity bode plots Figure 5.9 using Havriliak_Negami(HN) model[243]. The relaxation time for dielectric breakdown can vary depending on several factors such as the material of the dielectric, the magnitude of the electric field applied, and the environmental conditions. Generally, the relaxation time for dielectric breakdown refers to the time it takes for the dielectric material to recover its insulating properties after experiencing breakdown due to the application of a high electric field. This relaxation process typically involves mechanisms such as recombination of charge carriers, migration of ions, and thermal effects within the dielectric material. The time scale for these processes can range from microseconds to seconds or even longer, depending on the specific properties of the material and the conditions of the breakdown event. For practical applications and safety considerations, it's essential to understand the relaxation time of a dielectric material to prevent premature breakdown and ensure the reliability of electrical devices and systems. In the pristine sample, the relaxation time has decreased from micro seconds to fermi seconds with the rise in temperature.

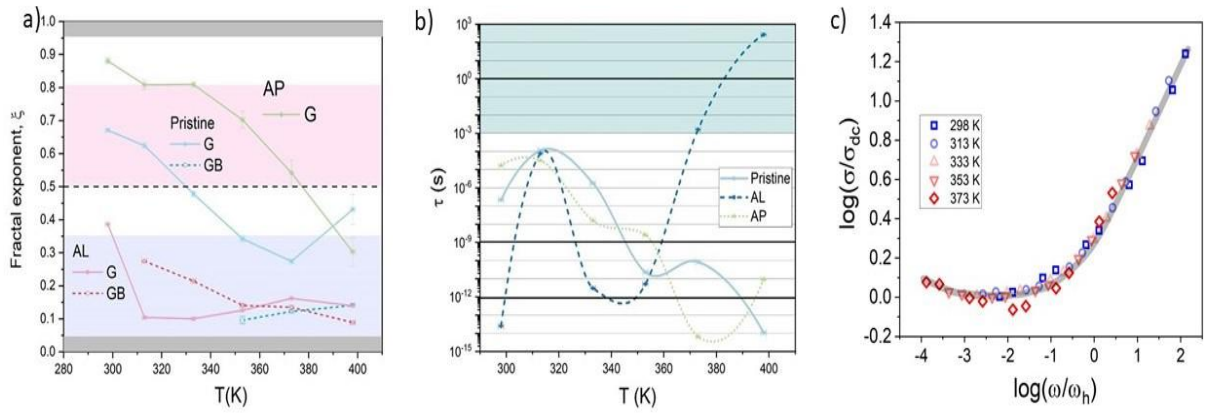

Figure 5.8 a) Fractal exponent variation with temperature for pristine, after light and freezed samples, (b) Variation of relaxation time with temperature for the studied samples (c) Ghosh scaling for the freezed charge carrier sample

While, the sample with light exposure, has shown a slow process where relaxation time has increased to ks. Again in the freezed samples, relaxation process is faster as similar to the pristine samples. This freezed process has been studied through Ghosh scaling and can be seen (in Figure 5.8c) that the charge carriers follow time temperature superposition principle (TTSP) while the pristine and after light samples do not follow TTSP Figure 5.10 [244].

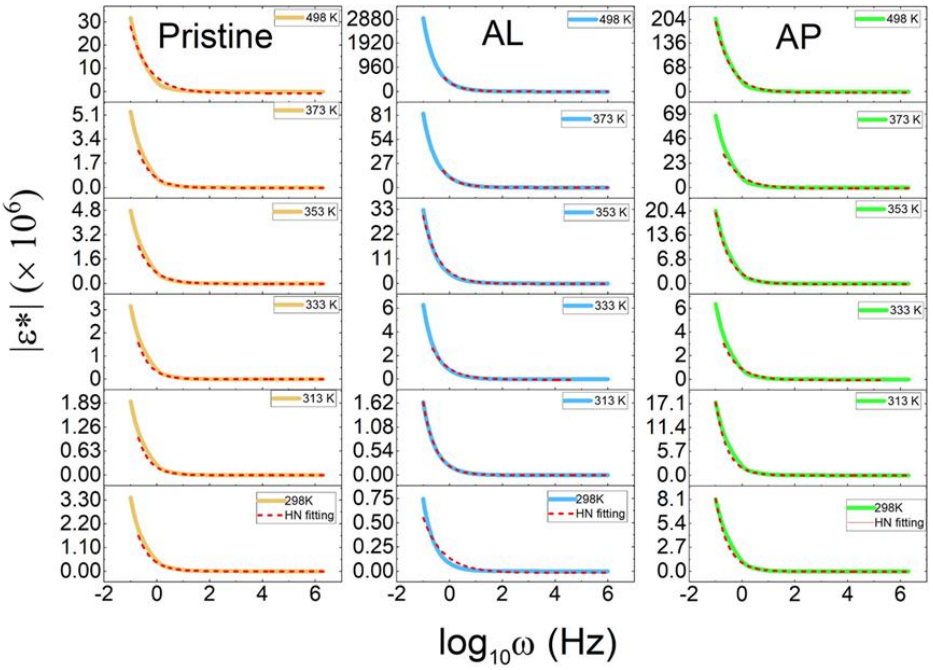

Figure 5.9 Havriliak–Negami (HN) fitted permittivity bode plots for pristine sample, after light (AL) treatment (IV measurement) and after poling (AP).

In the phonon spectrum, the normal vibrations of T_h group at Γ− point decompose into vibrational, acoustic and optical vibrations. 117 fundamental vibration modes decompose to 60 Raman active modes (-$5A^+$, $5E^+$($5B^+_1$, B^+_2) and $15F^+$), 42 infra-red (IR) active modes and 15 modes which are neither active in IR nor Raman spectra. The Raman spectra with the variation of temperature is shown in Figure 5.11. A^+ and E^+ modes are observed in x(zz)y polarizations. We have observed $(B^+_2)_3$, tr, E^+_2, F^+, A^+ and F^+ marked at positions

$\omega1, \omega2, \omega3, \omega5$ and $\omega6$, respectively correspond to Sn-I [245]. Further, E_g modes corresponding to Cs-I bond are marked at $\omega4$ and $\omega7$ [246]. With the increase in temperature at 325 K, vibrational frequency for A^{+}_{2}mode increases Fig. 5.12. Whereas, a blue shift in E_g modes corresponding to Cs-I modes is observed at 325 K Fig.5.13. On account of half-width, there is a sudden discontinuity at 325 K i.e. half-width of E_g modes corresponding to Cs-I modes has reduced whereas modes of Sn-I have shown increment in half-width at 325 K.

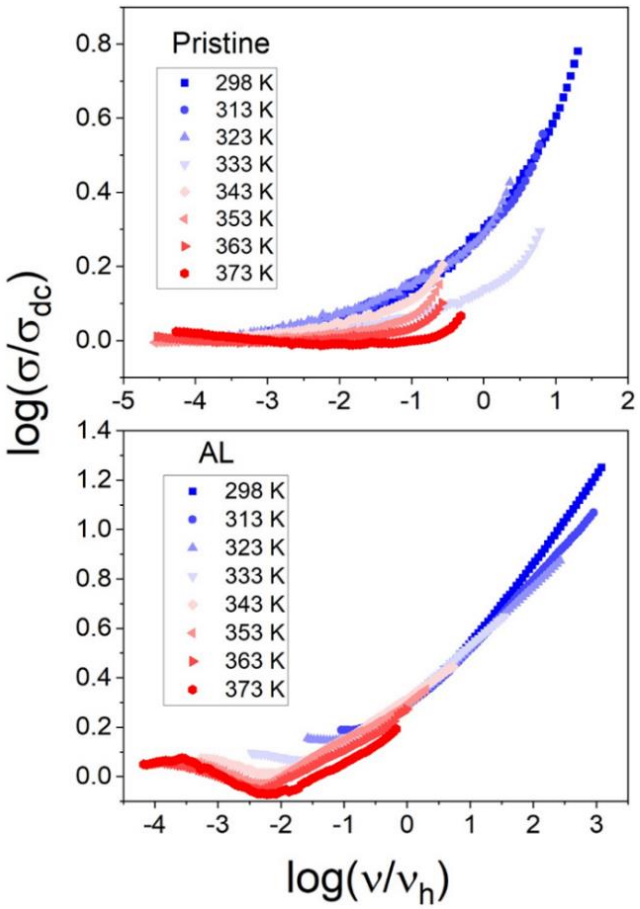

Figure 5.10 Ghosh scaling for pristine sample, and after light (AL) I-V measurement

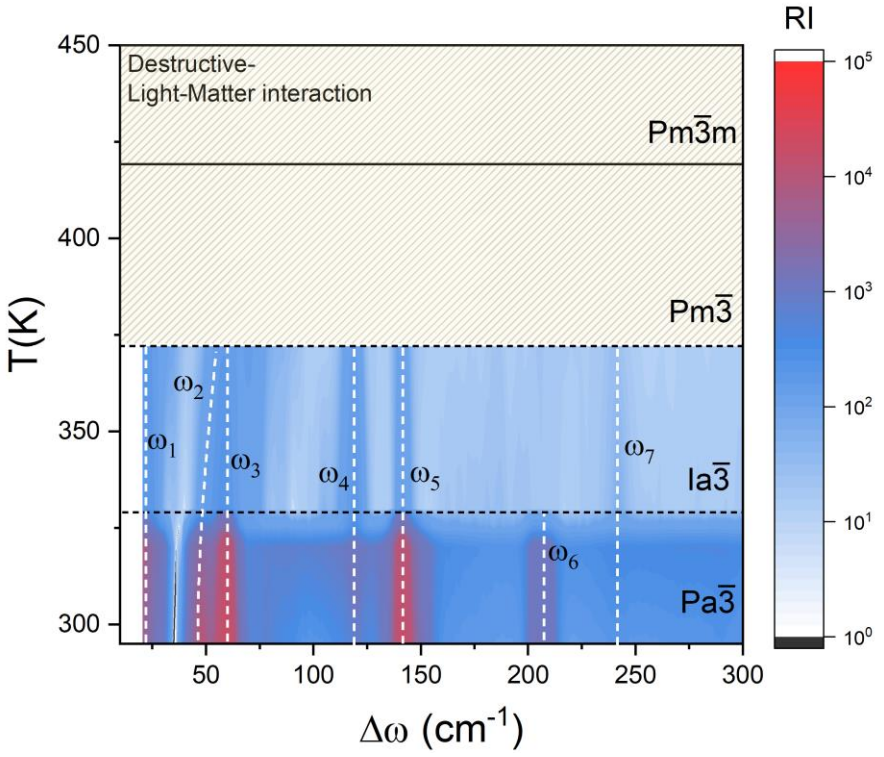

Figure 5.11 Raman spectrum with the variation of temperature for $CsSnI_{3\,000}$We have observed $(B^{+}{}_{2})_3$, tr, $E^{+}{}_{2}$, F^{+}, A^{+} and F^{+} marked at positions ω_1, ω_2, ω_3, ω_5 and ω_6, respectively correspond to Sn-I. Further, E_g modes corresponding to Cs-I bond are marked at ω_4 and ω_7.

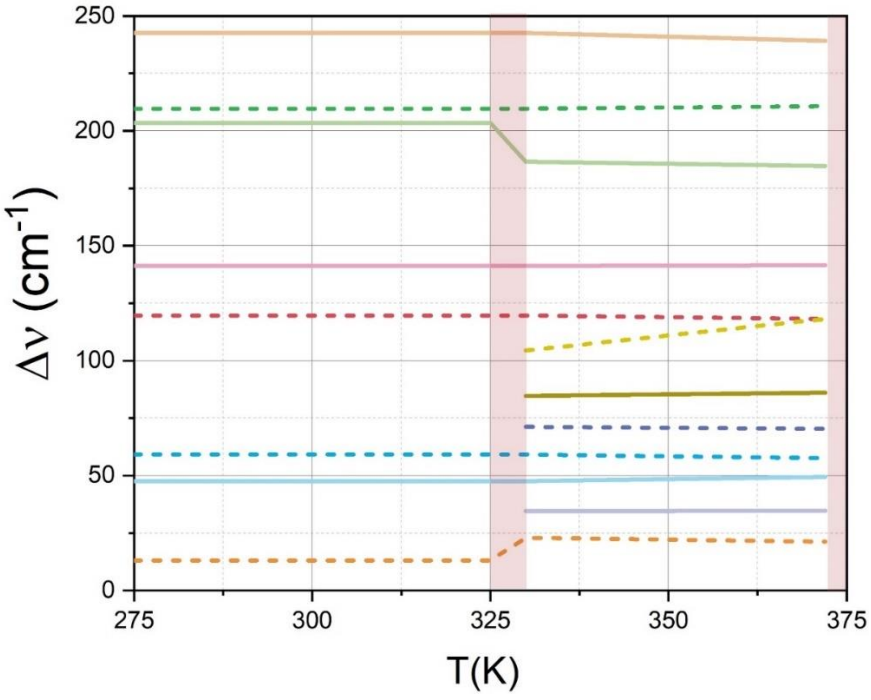

Figure 5.12 Raman shift with variation Temperature

The A^+ mode corresponds to the free SnI_4 molecule, the E_2^+ represents double degenerated E modes, $\omega 3$ represents 3-fold degenerated F_2 mode and deformation vibration by bended molecular valence bonds while $\omega 6$ corresponds to 3-fold degenerated F_2 mode and normal vibration through extended molecule valence bonds [247]. Now, with the changes in crystal environment, molecule equilibrium changes as compared to the free state.

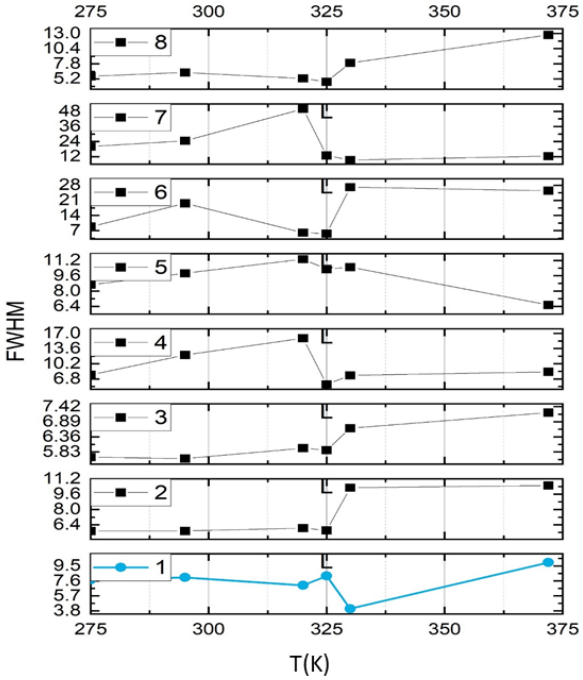

Figure 5.13 FWHM Raman peaks with variation of Temperature.

A small SnI_4 tetrahedron distortion has leads to the splitting of F_2 symmetry vibration modes with temperature. However, the static field effects in SnI are connected with the position symmetry of SnI molecules in the lattice. We have not observed the splitting of E-mode with temperature due to the orientation effect which comes into play upon the turning down of crystal lattice along z-axis. Thus, the normal vibration can be seen as linear combinations of SnI molecule displacements with their orientation conditioned by weak resonant Van der

Waals intramolecular interactions. Furthermore, Raman intensity, $I_R(=I_i\int_\Omega|< E_j \alpha E_i >|^2\ d\Omega)$ reduces at $Ia\bar{3}/Pa\bar{3}$ isomorphic phase transition and therefore polarizability, especially electronic polarizability α_e (coupled with $\triangle P_e$) should be reduced.

The splitting of vibration modes is observed in the high-frequency regions of the Raman spectra, leading to slight displacements of Raman line positions in the x(zz)y and x(zx)y polarizations in the low-frequency region. The low-frequency part of the Raman spectra of SnI_4 tetrahedra, with wavenumbers ranging from 0 to 50 cm^{-1}, is of particular interest. In the x(zz)y polarization, there are four lines in this region at 25.3 (23.9; 25.3), 29.8, 34.8, and 39.5 cm^{-1} (Figure 5.11). These lines correspond to vibrational modes associated with the rotational and translational modes of a free SnI_4 molecule. Specifically, two of these lines, 25.3 (23.9, 25.3) and 29.8 cm^{-1}, correspond to translational modes. The other two lines, 34.8 and 39.5 cm^{-1}, increase in intensity much faster with the exciting wavelength, corresponding to vibrational modes associated with rotational modes. The splitting of the 25.3 cm^{-1} line into two lines at 23.9 and 25.3 cm^{-1}, which corresponds to translational modes, is attributed to the decomposition of two degenerate translational E symmetry modes of the molecule in the C_{3v} group into translational B_1 and B_2 symmetry modes in the C_3 group. Similarly, the F_2 symmetry free molecule modes are assumed to split in the crystal field, with the lower vibrational frequencies corresponding to E symmetry modes. A notable feature of the low-frequency spectrum in Snl4 tetrahedra is that the F-symmetry acoustic and translational modes of the crystal correlate with the free molecule's F_2 symmetry translational mode, forming linear combinations of two Davydov multiples' F-symmetry components that correlate with A^+ and E symmetry translational modes of the molecule, deformed by the crystal field. This

additional mixing of modes can be obtained by constructing the normal Sn lattice vibrations from the components of the Davydov multiples.

5.4 Conclusion

In summary, we report the green polymorph of $CsSnI_3$ synthesized using Cold-sintering. At 295 K, this green polymorph $CsSnI_3$ possesses cubic structure with $Pa\bar{3}$ symmetry and direct band gap of 1.24 eV. Our study suggests that the green polymorph of $CsSnI_3$ is non-perovskite due to the presence of distorted SnI_3 tetrahedra, iodine atoms that are not in equivalent positions and the tetrahedra translation occurring along the threefold axis. Interestingly, this green-$CsSnI_3$ shows unusual successive isomorphic phase transitions.

Further, this work suggests that the local alteration in vibration modes significantly affects the current-voltage hysteresis and conduction behaviour of perovskite halides, indicating the presence of local non-Centro symmetry within the globally centrosymmetric $CsSnI_3$